

Tunable electron-electron interaction and anomalous enhancement of large-momentum scattering in moiré superlattices

Taiki Sato* and Hiroaki Ishizuka†

Department of Physics, Institute of Science Tokyo, Meguro, Tokyo 152-8551.

(Dated: March 18, 2025)

Using a microscopic model, we show that the electron-electron interaction of flat bands deviates significantly from the Coulomb interaction. In particular, we find that large-momentum scattering is enhanced at $\theta \lesssim 4^\circ$, with a non-monotonic momentum dependence appearing near the magic angle. For $\theta \gtrsim 1.2^\circ$, the enhanced large-momentum scattering can be attributed to the compact Wannier function. On the other hand, for $\theta \lesssim 1.2^\circ$, the nonmonotonic momentum dependence of the interaction matrix cannot be explained by a simple Wannier orbital, indicating a nontrivial modification to the el-el interaction. Notably, the range of angles θ where the large-momentum scattering is enhanced differs from the magic angles at which nearly-flat bands emerge, suggesting that the angle dependence of material properties provides information about the effect of interaction. The results highlight unusual features of the interaction in moiré graphene.

I. INTRODUCTION

Electron-electron interactions give rise to rich phases of matter, including Mott insulating, superconducting, and magnetic states. A compelling realization of such a correlated system is twisted van der Waals heterostructures [Fig.1(a)], in which the high tunability of electronic bands allows realizing flat bands that relatively enhance the electron-electron (el-el) interaction [1–7]. The existence of these narrow electronic bands, initially predicted theoretically, has since been confirmed experimentally [8–10]. Furthermore, recent experiments have revealed a variety of correlated phases in these systems, including superconductivity [11–15], ferromagnetism [16, 17], integer and fractional Chern insulating phases [18–20], nematicity [21–23], and charge order [24]. These discoveries highlight twisted moiré systems as a promising platform for studying and engineering electron correlations.

The behavior of strongly correlated systems is generally sensitive to both the form and strength of the effective el-el interaction. In moiré graphene, theoretical studies have suggested that el-el interactions play a significant role in shaping electronic states, even at the mean-field level [25–27], and that a heavy-fermion-like description may be relevant for the flat bands [28, 29]. Beyond the mean-field theory, sophisticated numerical methods have provided further insights into the correlation effects in these systems [30, 31], reinforcing the idea that electronic states and their dynamics are highly sensitive to the el-el interaction. Experimentally, a large T -linear resistivity has been observed over a range of twist angles, including those away from the magic angle [32–34], while a large T^2 -resistivity has been reported near full filling [35]. These transport behaviors have been attributed to enhanced electron-phonon and el-el interactions [36–38]. The pronounced sensitivity of moiré graphene to

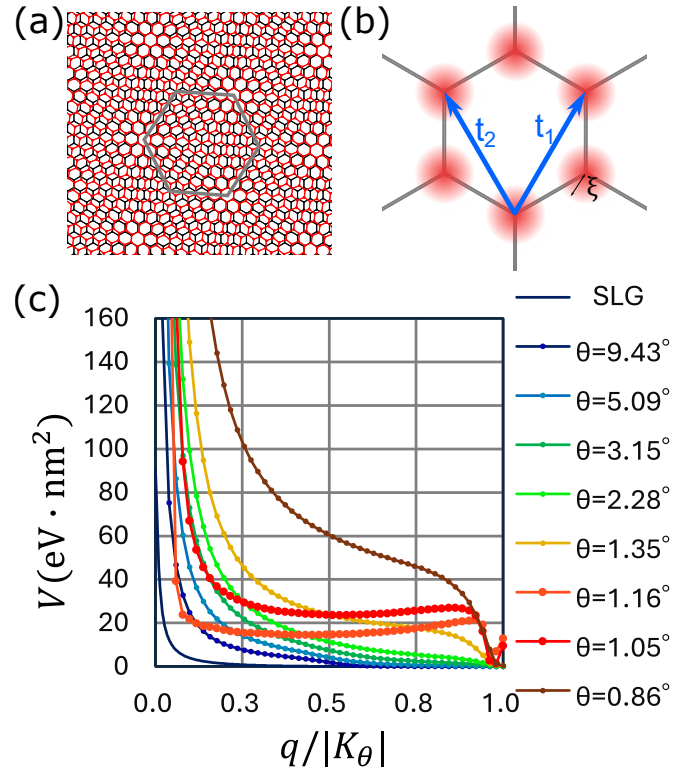


FIG. 1. Schematic of a moiré structure and the momentum dependence of electron-electron interaction matrix. Schematics of (a) the lattice structure of twisted bilayer graphene for $\theta = 7.34^\circ$, and (b) a tight-binding model taking account of small Wannier orbital radius. (c) The q dependence of the interaction matrix for the flat bands and the interaction matrix for pristine graphene along path A. The path along which the interaction matrices were calculated is given in Fig. 2(a).

the nature of interaction provides a unique opportunity to explore the relationship between correlated phases and the nature of el-el interaction.

In this work, we investigate the el-el interaction in moiré graphene using a microscopic theory based on a tight-binding model [7, 39]. We show that, beyond its

* taiki-sato@stat.phys.titech.ac.jp

† ishizuka@hiroishizuka.com

magnitude, the structure of the el-el interaction matrix for the flat bands undergoes significant changes with the twist angle [Fig. 1(c)]. Specifically, we find that large-momentum scattering is enhanced compared to the bare Coulomb interaction and that the interaction matrix exhibits a nonmonotonic momentum dependence near the magic angle. Notably, the enhancement of large-momentum scattering at twist angles $\theta \lesssim 1.2^\circ$, with non-monotonic dependence q , cannot be explained by a simple Wannier orbital description, suggesting nontrivial modifications to the el-el interaction. Our results indicate that, in addition to the emergence of narrow electronic bands, moiré graphene hosts a highly nontrivial el-el interaction structure that is strongly influenced by the underlying Wannier orbitals, with potential implications for its correlated phases.

II. MODEL AND METHOD

A. Tight-binding model

To study the effective interaction matrix at different twist angles, we calculate the electronic bands of moiré graphene using a tight-binding model [7], focusing on commensurate twist angles θ . Moiré graphene consists of two layers of graphene, labeled 1 and 2, with layer 2 twisted by an angle θ with respect to layer 1.

The system is spatially periodic for certain twist angles, which are called commensurate twist angles, allowing us to apply Bloch's theorem. The primitive vectors $\mathbf{t}_1, \mathbf{t}_2$ of the periodic moiré lattice are characterized by two integers (n, m) , $\mathbf{t}_1 = -m\mathbf{a}_1 + (n+m)\mathbf{a}_2$, $\mathbf{t}_2 = (n+m)\mathbf{a}_1 - n\mathbf{a}_2$. Here, $\mathbf{a}_1 = (a_0, 0)$ and $\mathbf{a}_2 = (a_0/2, \sqrt{3}a_0/2)$ ($a_0 = 2.46$ Å) are the primitive vectors of the pristine graphene in layer 1. The twist angle of this model is $\theta = \arccos\left(\frac{n^2+4nm+m^2}{2(n^2+nm+m^2)}\right)$ and the reciprocal lattice vectors are $\mathbf{G}_1 = \frac{1}{N_c}(n\mathbf{g}_1 + (n+m)\mathbf{g}_2)$, $\mathbf{G}_2 = \frac{1}{N_c}((n+m)\mathbf{g}_1 + m\mathbf{g}_2)$, where $4N_c = 4(n^2 + nm + m^2)$ is the number of carbon atoms in the unit cell and \mathbf{g}_i are the reciprocal vectors of pristine graphene in layer 1; $\mathbf{a}_i \cdot \mathbf{g}_j = 2\pi\delta_{ij}$. To avoid confusion, we call the Brillouin zone of moiré superlattice the moiré Brillouin zone. The position of two K points in the moiré Brillouin zone reads $\mathbf{K}_1 = \frac{1}{3}(\mathbf{G}_1 + \mathbf{G}_2)$, $\mathbf{K}_2 = \frac{1}{3}(-\mathbf{G}_1 + 2\mathbf{G}_2)$. We note that the length of primitive vectors $|\mathbf{t}_\theta| = |\mathbf{t}_1| = |\mathbf{t}_2|$ and position vector of the K -points $|\mathbf{K}_\theta| = |\mathbf{K}_1| = |\mathbf{K}_2|$ depends on the twist angle.

To calculate the el-el interaction matrix, we consider a Hamiltonian $H = H_0 + H_I$, where H_0 and H_I are the single-particle and interaction terms of the Hamiltonian, respectively. The single-particle Hamiltonian H_0 is based on a transferrable tight-binding model for carbon atoms [7, 40], which we explained in the Supplemental Material [41] (see also references [7, 39, 40, 42] therein).

B. Interaction matrix

To investigate the nature of the el-el interaction, we calculated the interaction matrix for the flat bands. To this end, we consider the Yukawa interaction between the electrons,

$$H_I = \frac{1}{2} \sum_{\sigma, \sigma'} \int d^3r d^3r' \hat{\psi}^\dagger(\mathbf{r}, \sigma) \hat{\psi}(\mathbf{r}, \sigma) V(\mathbf{r} - \mathbf{r}') \hat{\psi}^\dagger(\mathbf{r}', \sigma') \hat{\psi}(\mathbf{r}', \sigma'). \quad (1)$$

Here, $\hat{\psi}(\mathbf{r}, \sigma)$ is the field operator for electrons at position \mathbf{r} and spin σ , and $V(\mathbf{r}) = \frac{e^2}{4\pi\epsilon_0} \frac{\exp(-q_0|\mathbf{r}|)}{|\mathbf{r}|}$ with $e < 0$ being the electron charge, ϵ_0 is the permittivity of vacuum, and q_0^{-1} is the screening length. The interaction $V(\mathbf{r})$ is equivalent to the Coulomb interaction if $q_0 = 0$. In the following, we take $q_0^{-1} = 10000$ Å.

First, we write the el-el interaction Hamiltonian in Eq. (1) using the density operator,

$$H_I = \frac{1}{2S} \sum_{\mathbf{q}} \tilde{V}(\mathbf{q}) \tilde{\rho}(-\mathbf{q}) \tilde{\rho}(\mathbf{q}), \quad (2)$$

where $\tilde{\rho}(\mathbf{q})$ and $\tilde{V}(\mathbf{q})$ are the Fourier transform of the density operator $\hat{\rho}(\mathbf{r}) = \sum_{\sigma} \hat{\psi}^\dagger(\mathbf{r}, \sigma) \hat{\psi}(\mathbf{r}, \sigma)$ and $V(\mathbf{r})$, respectively, \mathbf{q} is the momentum, and S is the system size. Using the annihilation (creation) operator for the electrons in n th band with momentum \mathbf{k} , $\hat{c}_{n,\mathbf{k}}$ ($\hat{c}_{n,\mathbf{k}}^\dagger$), and its eigenstate wavefunction $\phi_{n,\mathbf{k}}$, calculated using a tight-binding model [7], the density operator in the momentum space reads

$$\tilde{\rho}(\mathbf{q}) = \sum_{n,m,\mathbf{k}} \langle \phi_{n,\mathbf{k}-\mathbf{q}} | e^{-i\mathbf{q} \cdot \hat{\mathbf{r}}} | \phi_{m,\mathbf{k}} \rangle \hat{c}_{n,\mathbf{k}-\mathbf{q}}^\dagger \hat{c}_{m,\mathbf{k}}, \quad (3)$$

where $\bar{\mathbf{k}}$ represents the momentum vector in the first moiré Brillouin zone that is equivalent to \mathbf{k} , and $\hat{\mathbf{r}}$ is the position operator. Using Eq. (3), the interaction Hamiltonian reads

$$H_I = \frac{1}{2S} \sum_{\substack{n,n',m,m' \\ \mathbf{k},\mathbf{k}',\mathbf{q}}} V_{\mathbf{k},\mathbf{k}',\mathbf{q}}^{n,n',m,m'} \hat{c}_{n',\mathbf{k}'+\mathbf{q}}^\dagger \hat{c}_{m',\mathbf{k}'}^\dagger \hat{c}_{n,\mathbf{k}-\mathbf{q}} \hat{c}_{m,\mathbf{k}}, \quad (4)$$

where

$$V_{\mathbf{k},\mathbf{k}',\mathbf{q}}^{n,n',m,m'} = \sum_{\mathbf{q}'=\mathbf{q}} \tilde{V}(\mathbf{q}') \langle \phi_{n',\mathbf{k}'+\mathbf{q}'} | e^{i\mathbf{q}' \cdot \hat{\mathbf{r}}} | \phi_{m',\mathbf{k}'} \rangle \times \langle \phi_{n,\mathbf{k}-\mathbf{q}'} | e^{-i\mathbf{q}' \cdot \hat{\mathbf{r}}} | \phi_{m,\mathbf{k}} \rangle, \quad (5)$$

is the interaction matrix. In Eq. (5), the sum is taken over all momenta \mathbf{q}' which are equivalent to \mathbf{q} in the first moiré Brillouin zone.

To compute Eq (5), we assumed that the p_z orbitals of carbon atoms are well localized on each site. In the momentum space representation, the eigenstate of H_0 reads

$|\phi_{n,\mathbf{k}}\rangle = \sum_{\mathbf{G},\alpha,l} \phi_{n,\mathbf{k}}(\mathbf{G},\alpha,l)|\mathbf{k} + \mathbf{G},\alpha,l\rangle$, where \mathbf{G} denotes reciprocal lattice vectors, $|\mathbf{k},\alpha,l\rangle = \sqrt{\frac{4}{N_{\text{atom}}}} \sum_n \exp(i\mathbf{k} \cdot \mathbf{r}_{n,\alpha}) |p_z(\mathbf{r} - \mathbf{r}_{n,\alpha,l})\rangle$, and $|p_z(\mathbf{r} - \mathbf{r}_{n,\alpha,l})\rangle$ is the wavefunction of the p_z orbital on the α th sublattice in the n th unit cell of the layer l , and N_{atom} represents the number of carbon atoms. For the localized p_z orbitals, i.e. $\langle p_z(\mathbf{r} - \mathbf{r}_{n,\alpha,l}) | e^{-i\mathbf{q} \cdot \mathbf{r}} | p_z(\mathbf{r} - \mathbf{r}_{m,\beta,l'}) \rangle \approx \delta_{nm} \delta_{\alpha\beta} \delta_{ll'} \langle p_z(\mathbf{r} - \mathbf{r}_{n,\alpha,l}) | e^{-i\mathbf{q} \cdot \mathbf{r}} | p_z(\mathbf{r} - \mathbf{r}_{n,\alpha,l}) \rangle$, the brackets in Eq. (5) become

$$\begin{aligned} \langle \phi_{n,\mathbf{k}-\mathbf{q}} | e^{-i\mathbf{q} \cdot \mathbf{r}} | \phi_{m,\mathbf{k}} \rangle &= \langle p_z(\mathbf{r}) | e^{-i\mathbf{q} \cdot \mathbf{r}} | p_z(\mathbf{r}) \rangle \\ &\times \sum_{\mathbf{G},\alpha,l} \phi_{m,\mathbf{k}}(\mathbf{G} - \mathbf{G}_{\mathbf{k}-\mathbf{q}} + \mathbf{g}^{(l)}, \alpha, l) \\ &\times \phi_{n,\mathbf{k}-\mathbf{q}}^*(\mathbf{G}, \alpha, l) e^{i\mathbf{g}^{(l)} \cdot \delta_{\alpha}^{(l)}}, \end{aligned} \quad (6)$$

where $\mathbf{g}^{(l)}$ is the reciprocal vector of the l th layer in the moiré graphene such that the wave number $\mathbf{G} - \mathbf{G}_{\mathbf{k}-\mathbf{q}} + \mathbf{g}^{(l)}$ is in the first Brillouin zone of pristine graphene in layer l , and $\mathbf{G}_{\mathbf{k}} = \mathbf{k} - \bar{\mathbf{k}}$ is a vector on the reciprocal lattice that relates \mathbf{k} and the equivalent wavenumber in the first moiré Brillouin zone $\bar{\mathbf{k}}$.

III. RESULTS

A. Electron-electron interaction

Typical \mathbf{q} dependence of $|V_{\mathbf{k},\mathbf{k}',\mathbf{q}}^{n,n',m,m'}|$ for the flat bands is plotted in Fig. 2(b) and 2(c). The flat bands consist of four conduction and valence bands, each of which corresponds to different spins and valley degrees of freedom [43–45]. Focusing on one of the two spin sectors, we label the two valence bands $n = 1, 2$, and the conduction bands $n = 3, 4$; the valence (conduction) bands $n = 1$ and 2 ($n = 3$ and 4) belong to different valleys of pristine graphene, as shown in Fig. 2(a). Figures 2(b)–2(d) shows the result of $|V_{\mathbf{k},\mathbf{k}',\mathbf{q}}^{3,4,3,4}|$ along the paths in the inset of Fig. 2(b). In the figures, \mathbf{k} and \mathbf{k}' are fixed to the wavenumbers corresponding to the two ends of the path, and the direction of \mathbf{q} is along the path as shown in Fig. 2(b). Figures 2(b) and 2(c) shows that, for most θ , $|V_{\mathbf{k},\mathbf{k}',\mathbf{q}}^{3,4,3,4}|$ decays monotonically with increasing $q = |\mathbf{q}|$, similar to that of the Coulomb interaction. Among the three results, the amplitude of $|V_{\mathbf{k},\mathbf{k}',\mathbf{q}}^{3,4,3,4}|$ for path A is smaller than those for paths B and C. This suppression resembles the suppression of backscattering in the Dirac electrons. The results are similar for other $|V_{\mathbf{k},\mathbf{k}',\mathbf{q}}^{n,n',m,m'}|$, as shown in the Supplemental Material [41].

On the other hand, $V_{\mathbf{k},\mathbf{k}',\mathbf{q}}^{n,n',m,m'}$ along paths A and C show nonmonotonic q dependence near the magic angle, as seen in the results for $\theta = 1.05^\circ$ in Fig. 2(d). The results show that the large angular momentum by the el-el interaction is enhanced near the magic angle, indicating a unique feature of the el-el interaction in moiré

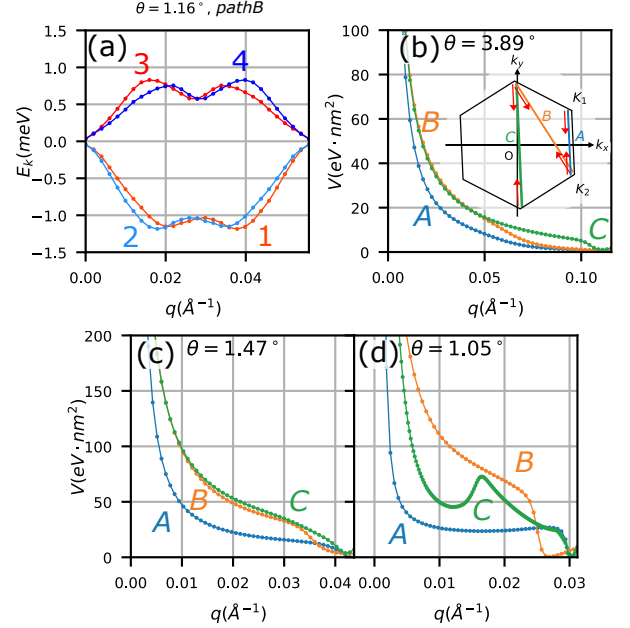


FIG. 2. The band and interaction matrix of electron-electron interaction. (a) The dispersion $E_{\mathbf{k}}$ of flat bands $n = 1, 2, 3, 4$ for twist angle $\theta = 1.16^\circ$ calculated along the path B (see inset of (b)). The even and odd bands belong to different valleys. The interaction matrix for twist angles (b) $\theta = 3.89^\circ$, (c) 1.47° , and (d) 1.05° . Inset of (b) shows three paths along which the interaction matrix was calculated: (A) $\mathbf{k} = 29/30\mathbf{K}_1 + 1/30\mathbf{K}_2$ and $\mathbf{k}' = 1/30\mathbf{K}_1 + 29/30\mathbf{K}_2$, (B) $\mathbf{k} = 29/30\mathbf{K}_1 - 28/30\mathbf{K}_2$ and $\mathbf{k}' = 1/30\mathbf{K}_1 + 28/30\mathbf{K}_2$, and (C) $\mathbf{k} = 29/30\mathbf{K}_1 - 28/30\mathbf{K}_2$ and $\mathbf{k}' = -28/30\mathbf{K}_1 + 29/30\mathbf{K}_2$. In all cases, the direction of \mathbf{q} is taken so that $\bar{\mathbf{k}} - \mathbf{q}$ moves from \mathbf{k} to \mathbf{k}' .

graphene. The enhancement of large momentum scattering is consistent with what is predicted in a previous work [37]. However, the nonmonotonic q dependence was not predicted. As shown in Fig. 1(c), the enhanced large-momentum scattering is seen in a range of angles around $\theta = 1.1^\circ$.

B. Twist-angle dependence

For a better understanding of the el-el interaction, we compare the results in Fig. 2 to a tight-binding model on a moiré honeycomb lattice. We consider a tight-binding model with one orbital on each site, and the Wannier function of the orbital is given by $w(\mathbf{r})$ [Fig. 1(b)]. The single-particle part of the Hamiltonian reads

$$\tilde{H}_0 = \sum_{\mathbf{k}} (\hat{\psi}_{\mathbf{k},1}^\dagger, \hat{\psi}_{\mathbf{k},2}^\dagger) \begin{pmatrix} 0 & h_{\mathbf{k}} \\ h_{\mathbf{k}}^* & 0 \end{pmatrix} \begin{pmatrix} \hat{\psi}_{\mathbf{k},1} \\ \hat{\psi}_{\mathbf{k},2} \end{pmatrix}, \quad (7)$$

where $h_{\mathbf{k}} = t \sum_{i=1}^3 e^{i\mathbf{k} \cdot \Delta_i}$ with t being the nearest neighbor hopping, Δ_i is vector connecting the three nearest neighbor sites in honeycomb lattice, and $\hat{\psi}_{\mathbf{k},a}$ ($\hat{\psi}_{\mathbf{k},a}^\dagger$) is

annihilation (creation) operator for the state $\psi_{\mathbf{k},a}(\mathbf{r}) = \frac{1}{\sqrt{N_{\text{UC}}}} \sum_n e^{i\mathbf{k} \cdot \mathbf{R}_{n,a}} w(\mathbf{r} - \mathbf{R}_{n,a})$ on sublattice $a = 1, 2$; the sum is taken over all unit cells $\mathbf{R}_{n,a}$, and N_{UC} is the number of moire unit cells. The eigenstates of \tilde{H}_0 reads

$$\psi_{\mathbf{k},\pm}(\mathbf{r}) = \frac{1}{\sqrt{2}} (g_{\mathbf{k}} \psi_{\mathbf{k},1}(\mathbf{r}) \pm \psi_{\mathbf{k},2}(\mathbf{r})), \quad g_{\mathbf{k}} = \frac{h_{\mathbf{k}}}{|h_{\mathbf{k}}|} \quad (8)$$

where \pm denotes the eigenstates for conduction and valence bands, respectively. Using the eigenstate basis and assuming that the Wannier function is well localized, i.e., $\langle w(\mathbf{r} - \mathbf{R}_{n,a}) | e^{i\mathbf{q} \cdot \mathbf{r}} | w(\mathbf{r} - \mathbf{R}_{m,b}) \rangle \approx \delta_{nm} \delta_{ab} \langle w(\mathbf{r} - \mathbf{R}_{n,a}) | e^{i\mathbf{q} \cdot \mathbf{r}} | w(\mathbf{r} - \mathbf{R}_{n,a}) \rangle$, the interaction matrix of electrons in the conduction band reads

$$V_{\mathbf{k},\mathbf{k}',\mathbf{q}}^{a,b,c,d} = e^{i(\mathbf{k}-\mathbf{k}'-\mathbf{q}+\mathbf{k}'-\mathbf{k}'+\mathbf{q}) \cdot \Delta_1} \times \sum_{\mathbf{q}'=\mathbf{q}} \tilde{V}(\mathbf{q}') |\eta_{\mathbf{q}'}|^2 \frac{g_{\mathbf{k}-\mathbf{q}'}^* g_{\mathbf{k}} + ac}{2} \frac{g_{\mathbf{k}'+\mathbf{q}'}^* g_{\mathbf{k}'} + bd}{2} \quad (9)$$

where $\eta_{\mathbf{q}} = \int d^2\mathbf{r} |w(\mathbf{r})|^2 e^{i\mathbf{q} \cdot \mathbf{r}}$ and $a, b, c, d = \pm 1$ denotes the bands. For electron-phonon interaction, a model similar to this model is known to reproduce the momentum dependence of the interaction matrix in moiré graphene [36].

Here, we consider the Yukawa interaction $\tilde{V}(\mathbf{q}) = \frac{e^2}{2\epsilon} \frac{1}{\sqrt{q_{\text{TF}}^2 + \mathbf{q}^2}}$ and a Gaussian Wannier function $w(\mathbf{r}) = \frac{1}{\sqrt{\pi} \xi_G} e^{-\mathbf{r}^2/2\xi_G^2}$ (an exponentially decaying Wannier function gives results similar to those of the Gaussian Wannier function, as shown in the Supplemental Material [41]). ϵ is the electrical permittivity, q_{TF}^{-1} is the Thomas-Fermi screening length, and ξ_G is the orbit radius of the Gaussian Wannier function. For the Gaussian Wannier function, the factor $\eta_{\mathbf{q}}$ in Eq. (9) reads $|\eta_{\mathbf{q}}|^2 = e^{-\frac{q^2 \xi_G^2}{2}}$. Hence, the large- q scattering channels, which include the large angle scatterings, are suppressed exponentially by increasing ξ_G .

Figures 3(a) and 3(b) shows the interaction matrix of conduction bands $V_{\mathbf{k},\mathbf{k}',\mathbf{q}}^{3,4,3,4}$ for $\theta = 1.35^\circ$ path A and $\theta = 1.47^\circ$ path B, respectively; they are calculated using the microscopic model (fb+) and a fitted interaction matrix using the effective tight-binding model (fit). The interaction matrix for the effective tight-binding model is obtained by fitting the results of the microscopic model using ϵ , q_{TF} , and ξ_G as the fitting parameters. The interaction matrix is well fitted by that of the effective tight-binding model in a wide range of q , as in Fig. 3(a) and Fig. 3(b). On the other hand, the sharp drop of $V_{\mathbf{k},\mathbf{k}',\mathbf{q}}^{3,4,3,4}$ near $q \sim 0.035 \text{ \AA}^{-1}$, is not reproduced in the fitted function. The discrepancy is presumably a consequence of an anticrossing of the conduction and valence bands in the microscopic model, as we show in [41]; such an anti-crossing is not present in the effective tight-binding model. Indeed, the interaction matrix between the conduction and valence bands, $V_{\mathbf{k},\mathbf{k}',\mathbf{q}}^{1,1,3,3}$, increases in

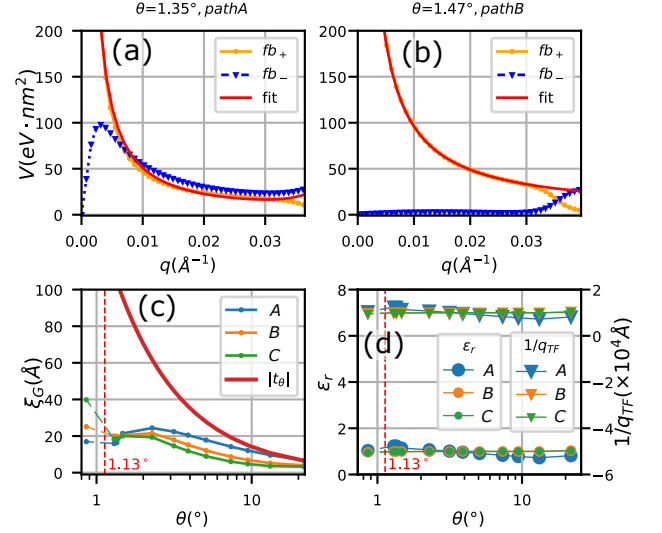


FIG. 3. Fitting of the interaction matrix for the flat bands by using a Gaussian Wannier function. (a,b) The interaction matrix corresponds to scattering from the conduction to the conduction band (fb+), the interaction matrix corresponds to scattering from the conduction to the valence band (fb-), and the fitting function for fb+ (fit). The results are for paths A (a) and B (b). (c) Angle dependence of radius ξ_G of Gaussian Wannier function calculated in three paths A, B, and C. The length of the primitive vector $|t_\theta|$ is also plotted. (d) The twist angle dependence of ϵ_r and $1/q_{\text{TF}}$ for the three paths. See the main text for details.

the $q \geq 0.03 \text{ \AA}^{-1}$, region as shown by the blue dots (fb-). Therefore, we fitted $V_{\mathbf{k},\mathbf{k}',\mathbf{q}}^{n,n',m,m'}$ excluding the large q region where a band crossing or an anticrossing occurs. With the treatment, we find that the interaction matrix for the effective tight-binding model reproduces the overall behavior of $V_{\mathbf{k},\mathbf{k}',\mathbf{q}}^{n,n',m,m'}$.

Figures 3(c) and 3(d) show the twist angle dependence of the fitting parameters. As shown in Fig. 3(d), relative permittivity ϵ_r and screening length $1/q_{\text{TF}}$ are almost a constant of the twist angle in the entire range of calculation. On the other hand, the orbital radius ξ_G shown in Fig. 3(c) changes by changing the twist angle. In most materials, the radius of the Wannier orbital scales linearly with $|t_\theta|$, in the case of which the dependence on the twist angle becomes $\xi_G \propto 1/\theta$ in the small θ limit. In contrast, the result in Fig. 3(c) shows that the radius is $\xi_G \leq |t_\theta|/3$ at the angles $\theta \lesssim 2^\circ$. It implies that the radius of Wannier orbitals becomes considerably small compared to the size of the unit cell. This is in agreement with that the large-angle scattering becomes relatively large in the small θ ($\gtrsim 1.2^\circ$) region near the first magic angle.

For the regions $1.0^\circ \lesssim \theta \lesssim 1.2^\circ$, on the other hand, we find that the interaction matrix shows a non-monotonic q dependence which cannot be reproduced using the Gaussian model. An example of the fitting is shown in the Supplemental Material [41]. The results demonstrate that the el-el interaction matrix shows unique features

not captured by a simple effective model with enhanced large q scatterings by the compact Wannier orbital.

In addition, we also calculated the interaction matrix for the high-energy bands. For them, the interaction matrix is well reproduced by the effective model, and ξ_G is more than twice as large as that for the flat bands at the same twist angle at $\theta \lesssim 2.0^\circ$, as shown in the Supplemental Material [41] (see also [46] therein). Hence, comparing the transport and other properties of moiré graphene in the flat and high-energy bands may provide evidence for the anomalous interaction matrix of the flat bands near the magic angle.

IV. CONCLUSION

In this work, we studied the electron-electron interaction matrix using a transferrable tight-binding model for carbon atoms and by constructing an effective tight-binding model. Using the transferrable tight-binding model, we find that the large- q scattering by electron-electron interaction is enhanced in the flat bands. For the twist angles $\theta \gtrsim 1.2$, the enhancement of large- q scattering is well reproduced by an effective tight-binding model on the honeycomb lattice with a compact Wannier function; the effective radius of the Wannier function is smaller than the unit cell, reaching below $1/4$ of the length of primitive vectors at $\theta < 2^\circ$. Such a Wannier orbital with a small radius would enhance the large- q scattering of electrons through a Purcell-effect-like enhancement [37]. On the other hand, for $\theta \lesssim 1.2^\circ$ we find a non-monotonic q dependence of the interaction matrix. Such a q dependence cannot be explained

by the effective tight-binding model, implying a strong enhancement of the large-angle scattering that cannot be captured with the simple effective model. As the enhancement of electron-electron interaction is seen only at small twist angles near the first magic angle, it is possibly related to the unusual properties of moiré graphene.

The enhancement of large- q scattering and unusual q dependence of electron-electron interaction found near the magic angle indicates that careful consideration of the interaction matrix might be necessary to understand the interaction physics of moiré graphene, in addition to the narrow bandwidth. The enhanced large- q scattering is likely to affect the transport properties by enhancing the scattering of electrons by the electron-electron interaction. Interestingly, such enhancement of the electron-electron interaction is seen below $\theta \sim 4^\circ$. This is different from the flat band formation, which is highly sensitive to the twist angle; the bandwidth is more than ten times larger than that of the magic angle at $\theta \sim 1.1^\circ$. Therefore, the twist-angle dependence of the material properties can be used to investigate the origin of the interaction physics in moiré graphene.

DATA AVAILABILITY

The data supporting this study's findings are available within the article and the Supplemental Material.

ACKNOWLEDGMENTS

This work was supported by JSPS KAKENHI (Grant No. JP23K03275) and JST PRESTO (Grant No. JPMJPR2452).

-
- [1] J. M. B. Lopes dos Santos, N. M. R. Peres, and A. H. Castro Neto, Graphene bilayer with a twist: Electronic structure, *Phys. Rev. Lett.* **99**, 256802 (2007).
 - [2] E. J. Mele, Commensuration and interlayer coherence in twisted bilayer graphene, *Phys. Rev. B* **81**, 161405 (2010).
 - [3] S. Shallcross, S. Sharma, E. Kandelaki, and O. A. Pankratov, Electronic structure of turbostratic graphene, *Phys. Rev. B* **81**, 165105 (2010).
 - [4] E. Suárez Morell, J. D. Correa, P. Vargas, M. Pacheco, and Z. Barticevic, Flat bands in slightly twisted bilayer graphene: Tight-binding calculations, *Phys. Rev. B* **82**, 121407 (2010).
 - [5] R. Bistritzer and A. H. MacDonald, Transport between twisted graphene layers, *Phys. Rev. B* **81**, 245412 (2010).
 - [6] R. Bistritzer and A. H. MacDonald, Moiré bands in twisted double-layer graphene, *Proc. Natl. Acad. Sci.* **108**, 12233 (2011).
 - [7] G. Trambly de Laissardiére, D. Mayou, and L. Magaud, Localization of dirac electrons in rotated graphene bilayers, *Nano Letters* **10**, 804–808 (2010).
 - [8] G. Li, A. Luican, J. M. B. Lopes dos Santos, A. H. Castro Neto, A. Reina, J. Kong, and E. Y. Andrei, Observation of van hove singularities in twisted graphene layers, *Nature Physics* **6**, 109 (2010).
 - [9] M. I. B. Utama, R. J. Koch, K. Lee, N. Leconte, H. Li, S. Zhao, L. Jiang, J. Zhu, K. Watanabe, T. Taniguchi, P. D. Ashby, A. Weber-Bargioni, A. Zettl, C. Jozwiak, J. Jung, E. Rotenberg, A. Bostwick, and F. Wang, Visualization of the flat electronic band in twisted bilayer graphene near the magic angle twist, *Nature Physics* **17**, 184 (2021).
 - [10] S. Lisi, X. Lu, T. Benschop, T. A. de Jong, P. Stepanov, J. R. Duran, F. Margot, I. Cucchi, E. Cappelli, A. Hunter, A. Tamai, V. Kandyba, A. Giampietri, A. Barinov, J. Jobst, V. Stalman, M. Leeuwenhoek, K. Watanabe, T. Taniguchi, L. Rademaker, S. J. van der Molen, M. P. Allan, D. K. Efetov, and F. Baumberger, Observation of flat bands in twisted bilayer graphene, *Nature Physics* **17**, 189 (2021).
 - [11] Y. Cao, V. Fatemi, S. Fang, K. Watanabe, T. Taniguchi, E. Kaxiras, and P. Jarillo-Herrero, Unconventional superconductivity in magic-angle graphene superlattices, *Nature* **556**, 43 (2018).
 - [12] Y. Cao, V. Fatemi, A. Demir, S. Fang, S. L. Tomarken, J. Y. Luo, J. D. Sanchez-Yamagishi, K. Watanabe,

- T. Taniguchi, E. Kaxiras, R. C. Ashoori, and P. Jarillo-Herrero, Correlated insulator behaviour at half-filling in magic-angle graphene superlattices, *Nature* **556**, 80 (2018).
- [13] X. Lu, P. Stepanov, W. Yang, M. Xie, M. A. Aamir, I. Das, C. Urgell, K. Watanabe, T. Taniguchi, G. Zhang, A. Bachtold, A. H. MacDonald, and D. K. Efetov, Superconductors, orbital magnets and correlated states in magic-angle bilayer graphene, *Nature* **574**, 653 (2019).
- [14] M. Yankowitz, S. Chen, H. Polshyn, Y. Zhang, K. Watanabe, T. Taniguchi, D. Graf, A. F. Young, and C. R. Dean, Tuning superconductivity in twisted bilayer graphene, *Science* **363**, 1059 (2019).
- [15] H. S. Arora, R. Polski, Y. Zhang, A. Thomson, Y. Choi, H. Kim, Z. Lin, I. Z. Wilson, X. Xu, J.-H. Chu, K. Watanabe, T. Taniguchi, J. Alicea, and S. Nadj-Perge, Superconductivity in metallic twisted bilayer graphene stabilized by wse₂, *Nature* **583**, 379 (2020).
- [16] A. L. Sharpe, E. J. Fox, A. W. Barnard, J. Finney, K. Watanabe, T. Taniguchi, M. A. Kastner, and D. Goldhaber-Gordon, Emergent ferromagnetism near three-quarters filling in twisted bilayer graphene, *Science* **365**, 605 (2019).
- [17] M. Serlin, C. L. Tschirhart, H. Polshyn, Y. Zhang, J. Zhu, K. Watanabe, T. Taniguchi, L. Balents, and A. F. Young, Intrinsic quantized anomalous hall effect in a moiré heterostructure, *Science* **367**, 900 (2020).
- [18] K. P. Nuckolls, M. Oh, D. Wong, B. Lian, K. Watanabe, T. Taniguchi, B. A. Bernevig, and A. Yazdani, Strongly correlated chern insulators in magic-angle twisted bilayer graphene, *Nature* **588**, 610 (2020).
- [19] Y. Choi, H. Kim, Y. Peng, A. Thomson, C. Lewandowski, R. Polski, Y. Zhang, H. S. Arora, K. Watanabe, T. Taniguchi, J. Alicea, and S. Nadj-Perge, Correlation-driven topological phases in magic-angle twisted bilayer graphene, *Nature* **589**, 536 (2021).
- [20] Y. Xie, A. T. Pierce, J. M. Park, D. E. Parker, E. Khalaf, P. Ledwith, Y. Cao, S. H. Lee, S. Chen, P. R. Forrester, K. Watanabe, T. Taniguchi, A. Vishwanath, P. Jarillo-Herrero, and A. Yacoby, Fractional chern insulators in magic-angle twisted bilayer graphene, *Nature* **600**, 439 (2021).
- [21] Y. Choi, J. Kemmer, Y. Peng, A. Thomson, H. Arora, R. Polski, Y. Zhang, H. Ren, J. Alicea, G. Refael, F. von Oppen, K. Watanabe, T. Taniguchi, and S. Nadj-Perge, Electronic correlations in twisted bilayer graphene near the magic angle, *Nature Physics* **15**, 1174 (2019).
- [22] A. Kerelsky, L. J. McGilly, D. M. Kennes, L. Xian, M. Yankowitz, S. Chen, K. Watanabe, T. Taniguchi, J. Hone, C. Dean, A. Rubio, and A. N. Pasupathy, Maximized electron interactions at the magic angle in twisted bilayer graphene, *Nature* **572**, 95 (2019).
- [23] Y. Cao, D. Rodan-Legrain, J. M. Park, N. F. Q. Yuan, K. Watanabe, T. Taniguchi, R. M. Fernandes, L. Fu, and P. Jarillo-Herrero, Nematicity and competing orders in superconducting magic-angle graphene, *Science* **372**, 264–271 (2021).
- [24] Y. Jiang, X. Lai, K. Watanabe, T. Taniguchi, K. Haule, J. Mao, and E. Y. Andrei, Charge order and broken rotational symmetry in magic-angle twisted bilayer graphene, *Nature* **573**, 91 (2019).
- [25] F. Guinea and N. R. Walet, Electrostatic effects, band distortions, and superconductivity in twisted graphene bilayers, *Proceedings of the National Academy of Sciences* **115**, 13174 (2018).
- [26] J. González and T. Stauber, Magnetic phases from competing hubbard and extended coulomb interactions in twisted bilayer graphene, *Phys. Rev. B* **104**, 115110 (2021).
- [27] A. Jimeno-Pozo, Z. A. H. Goodwin, P. A. Pantaleón, V. Vitale, L. Klebl, D. M. Kennes, A. A. Mostofi, J. Lischner, and F. Guinea, Short versus long range exchange interactions in twisted bilayer graphene, *Advanced Physics Research* **2**, 2300048 (2023).
- [28] Z.-D. Song and B. A. Bernevig, Magic-angle twisted bilayer graphene as a topological heavy fermion problem, *Phys. Rev. Lett.* **129**, 047601 (2022).
- [29] Y.-Z. Chou and S. Das Sarma, Kondo lattice model in magic-angle twisted bilayer graphene, *Phys. Rev. Lett.* **131**, 026501 (2023).
- [30] G. Rai, L. Crippa, D. Călugăru, H. Hu, F. Paoletti, L. de' Medici, A. Georges, B. A. Bernevig, R. Valentí, G. Sangiovanni, and T. Wehling, Dynamical correlations and order in magic-angle twisted bilayer graphene, *Phys. Rev. X* **14**, 031045 (2024).
- [31] Z.-Y. Xiao and S. Zhang, Correlation effects in magic-angle twisted bilayer graphene: An auxiliary-field quantum monte carlo study (2024), arXiv:2405.17808 [cond-mat.str-el].
- [32] T.-F. Chung, Y. Xu, and Y. P. Chen, Transport measurements in twisted bilayer graphene: Electron-phonon coupling and landau level crossing, *Phys. Rev. B* **98**, 035425 (2018).
- [33] H. Polshyn, M. Yankowitz, S. Chen, Y. Zhang, K. Watanabe, T. Taniguchi, C. R. Dean, and A. F. Young, Large linear-in-temperature resistivity in twisted bilayer graphene, *Nature Physics* **15**, 1011 (2019).
- [34] Y. Cao, D. Chowdhury, D. Rodan-Legrain, O. Rubies-Bigorda, K. Watanabe, T. Taniguchi, T. Senthil, and P. Jarillo-Herrero, Strange metal in magic-angle graphene with near planckian dissipation, *Phys. Rev. Lett.* **124**, 076801 (2020).
- [35] A. Jaoui, I. Das, G. Di Battista, J. Díez-Mérida, X. Lu, K. Watanabe, T. Taniguchi, H. Ishizuka, L. Levitov, and D. K. Efetov, Quantum critical behaviour in magic-angle twisted bilayer graphene, *Nature Physics* **18**, 633 (2022).
- [36] H. Ishizuka, A. Fahimniya, F. Guinea, and L. Levitov, Purcell-like enhancement of electron-phonon interactions in long-period superlattices: Linear-temperature resistivity and cooling power, *Nano Letters* **21**, 7465 (2021), PMID: 34515488.
- [37] H. Ishizuka and L. Levitov, Wide-range t₂ resistivity and umklapp scattering in moiré graphene, *New Journal of Physics* **24**, 052001 (2022).
- [38] J. D. Mehew, R. L. Merino, H. Ishizuka, A. Block, J. D. Mérida, A. D. Carlón, K. Watanabe, T. Taniguchi, L. S. Levitov, D. K. Efetov, and K.-J. Tielrooij, Ultrafast umklapp-assisted electron-phonon cooling in magic-angle twisted bilayer graphene, *Science Advances* **10**, ead1361 (2024).
- [39] G. Trambly de Laissardiére, D. Mayou, and L. Magaud, Numerical studies of confined states in rotated bilayers of graphene, *Phys. Rev. B* **86**, 125413 (2012).
- [40] C. H. Xu, C. Z. Wang, C. T. Chan, and K. M. Ho, A transferable tight-binding potential for carbon, *Journal of Physics: Condensed Matter* **4**, 6047 (1992).
- [41] See Supplemental Material at [url] for additional information on the interaction matrix: Tight-binding model,

- fitting by using the exponentially decaying Wannier function, fitting for the high energy band, the interaction matrix for each band, calculations for the suppression of backscattering in Dirac electrons, and illustrations of the fitting, which includes Ref [7, 39, 40, 42, 46].
- [42] J. C. Slater and G. F. Koster, Simplified lcao method for the periodic potential problem, *Phys. Rev.* **94**, 1498 (1954).
 - [43] M. Koshino, N. F. Q. Yuan, T. Koretsune, M. Ochi, K. Kuroki, and L. Fu, Maximally localized wannier orbitals and the extended hubbard model for twisted bilayer graphene, *Phys. Rev. X* **8**, 031087 (2018).
 - [44] J. Kang and O. Vafek, Symmetry, maximally localized wannier states, and a low-energy model for twisted bilayer graphene narrow bands, *Phys. Rev. X* **8**, 031088 (2018).
 - [45] S. Carr, S. Fang, Z. Zhu, and E. Kaxiras, Exact continuum model for low-energy electronic states of twisted bilayer graphene, *Phys. Rev. Res.* **1**, 013001 (2019).
 - [46] A. L. Shilov, M. A. Kashchenko, P. A. Pantaleón Peralta, Y. Wang, M. Kravtsov, A. Kudriashov, Z. Zhan, T. Taniguchi, K. Watanabe, S. Slizovskiy, K. S. Novoselov, V. I. Fal'ko, F. Guinea, and D. A. Bandurin, High-mobility compensated semimetals, orbital magnetization, and umklapp scattering in bilayer graphene moiré superlattices, *ACS Nano* **18**, 11769 (2024).

Supplemental Material to

“Tunable electron-electron interaction and anomalous enhancement of large-momentum scattering in moiré superlattices”

Taiki Sato¹ and Hiroaki Ishizuka¹

¹*Department of Physics, Tokyo Institute of Technology, Meguro, Tokyo, 152-8551, Japan*
(Dated: March 18, 2025)

I. TIGHT-BINDING MODEL

The single-particle Hamiltonian is based on a transferrable tight-binding model for carbon atoms [1, 2],

$$H_0 = \sum_{n,\alpha,l,m,\beta,l'} t(\mathbf{r}_{n,\alpha,l} - \mathbf{r}_{m,\beta,l'}) \hat{c}_{n,\alpha,l}^\dagger \hat{c}_{m,\beta,l'}. \quad (\text{S1})$$

Here, $\mathbf{r}_{n,\alpha,l}$ is the position vector of sublattice α in the n th unit cell in the l th layer, $\hat{c}_{n,\alpha,l}$ ($\hat{c}_{n,\alpha,l}^\dagger$) the annihilation (creation) operator for the electron in the p_z orbital of the atom at $\mathbf{r}_{n,\alpha,l}$, and

$$t(\mathbf{r}) = n_z(\mathbf{r})^2 t_{pp\sigma}(\mathbf{r}) + (1 - n_z(\mathbf{r})^2) t_{pp\pi}(\mathbf{r}). \quad (\text{S2})$$

is the hopping integral between two p_z orbitals at distance $\mathbf{r} = (x, y, z)$ [3]. In Eq. (S2), $n_z(\mathbf{r}) = z/|\mathbf{r}|$ is the direction cosine for the z axis, and

$$\begin{aligned} t_{pp\pi}(\mathbf{r}) &= -\gamma_0 \exp \left(q_\pi \left(1 - \frac{\sqrt{3}|\mathbf{r}|}{a_0} \right) \right), \\ t_{pp\sigma}(\mathbf{r}) &= \gamma_1 \exp \left(q_\sigma \left(1 - \frac{|\mathbf{r}|}{d} \right) \right). \end{aligned} \quad (\text{S3})$$

are the π and σ hopping integrals between the p_z orbitals, respectively [2]. Here, $\gamma_0 = 2.7$ eV is the nearest neighbor hopping integral of graphene, $\gamma_1 = 0.48$ eV is the inter-layer hopping integral between two vertically aligned carbon atoms, and $d = 3.35$ Å is the distance between the two layers of graphene. In the following, we use $q_\pi = \ln(10)/(\sqrt{3} - 1)$ and $q_\sigma = \sqrt{3}d q_\pi / a_0$, which reproduce the dispersion of pristine and bilayer graphene in the first-principles calculations [4].

II. EXPONENTIAL WANNIER FUNCTION

Here, we considered an exponentially decaying Wannier function $w(\mathbf{r}) = \sqrt{\frac{2}{\pi}} \frac{1}{\xi_E} e^{-r/\xi_E}$, where ξ_E is the orbital radius. Figure S1 shows an example of the fitting and the twist angle dependence of the fitted parameters. The results are similar to those of the Gaussian Wannier function.

III. ELECTRON-ELECTRON INTERACTION IN HIGH-ENERGY BANDS

We also considered the interaction matrix for the high-energy dispersive bands shown in Fig. S2(b). Experimentally, the filling of moiré materials is highly tunable, enabling doping of the bands above the flat bands [5]. As the θ dependence of the interaction matrix in the high-energy band is generally different from that of the low-energy bands, comparing the results of the flat bands to those of the high-energy bands may provide a way to experimentally investigate the enhancement of el-el interaction in the flat bands.

The interaction matrix of the high-energy bands is calculated in the same way as those of flat bands. For the fitting, we considered a triangular lattice tight-binding model with Gaussian Wannier function $w(\mathbf{r}) = \frac{1}{\sqrt{\pi}\xi_G} e^{-r^2/2\xi_G^2}$ since the band bottom of the high-energy band is usually at the Γ point and no Dirac nodes exist in the high-energy bands. The eigenstate wavefunction of the high-energy band reads $\psi_{\mathbf{k}}(\mathbf{r}) = \frac{1}{\sqrt{N}} \sum_n e^{i\mathbf{k} \cdot \mathbf{R}_n} w(\mathbf{r} - \mathbf{R}_n)$, where the sum

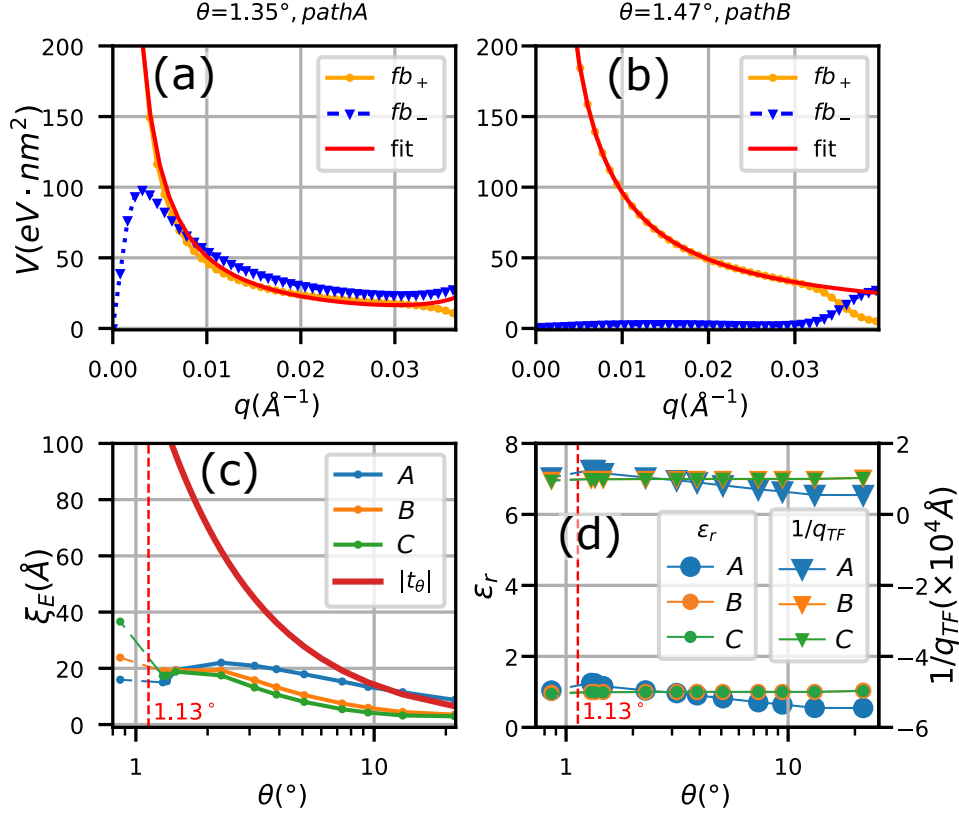


FIG. S1. Fitting of the interaction matrix for flat bands by using an exponential Wannier function. (a,b) The interaction matrix corresponds to scattering from the conduction to conduction band (fb_+), the interaction matrix corresponds to scattering from the conduction to valence band (fb_-), and the fitting function for fb_+ (fit). The results are for paths A (a) and B (b). (c) Angle dependence of radius ξ_E of exponential Wannier function calculated in three paths A, B, and C. The length of the primitive vector $|t_\theta|$ is also plotted. (d) Angle dependence of ϵ_r and $1/q_{TF}$ calculated in three paths. See the main text for details.

is taken over all lattice points \mathbf{R}_n in the triangle lattice. Using these results, the interaction matrix for high energy bands reads

$$V_{\mathbf{k},\mathbf{k}',\mathbf{q}}^{\text{HE}} = \sum_{\mathbf{q}'=\mathbf{q}} \tilde{V}(\mathbf{q}') |\eta_{\mathbf{q}'}|^2, \quad (\text{S4})$$

which we use for the effective tight-binding model.

Figure S2(a) shows the interaction matrix for $\theta = 1.3^\circ$ and $V_{\mathbf{k},\mathbf{k}',\mathbf{q}}^{\text{HE}}$. Unlike the case of flat bands, $V_{\mathbf{k},\mathbf{k}',\mathbf{q}}^{\text{HE}}$ shows a very small dependence on the paths. In addition, the overall form of $V_{\mathbf{k},\mathbf{k}',\mathbf{q}}^{\text{HE}}$ is well reproduced by the Coulomb interaction, except for angles where the fitting parameters were strongly affected by band crossings (see the section IV B). Similar to the result shown in Fig. S2(a), we find that the interaction matrix is well fitted by Eq. (S4) for all twist angles we considered.

Fig. S2(c) and Fig. S2(d) shows the twist angle dependence of the fitting parameters ξ_G , ϵ_r , and $1/q_{TF}$. Similarly to the case of flat bands, ϵ_r and $1/q_{TF}$ show very little dependence on the twist angle for the path A and path B below 2.5° . The upturn for the path B in the $\theta \gtrsim 2.5^\circ$ region is likely to be an artifact of the band crossings; we mainly focus on $\theta \lesssim 2.5^\circ$ as the multi-band effect complicates the analysis. On the other hand, ξ_G increases as the twist angle decreases, contrasting the flat-band case; ξ_G for the high-energy bands is more than twice as large as that for the flat bands at the same twist angle at $\theta \lesssim 2.0^\circ$. The larger ξ_G suppresses large- q scattering in the high-energy bands, suppressing the T^2 resistivity and other features related to the el-el interaction. Hence, comparing the transport and other properties of moiré graphene in the flat and high-energy bands may provide evidence for the anomalous interaction matrix of the flat bands near the magic angle.

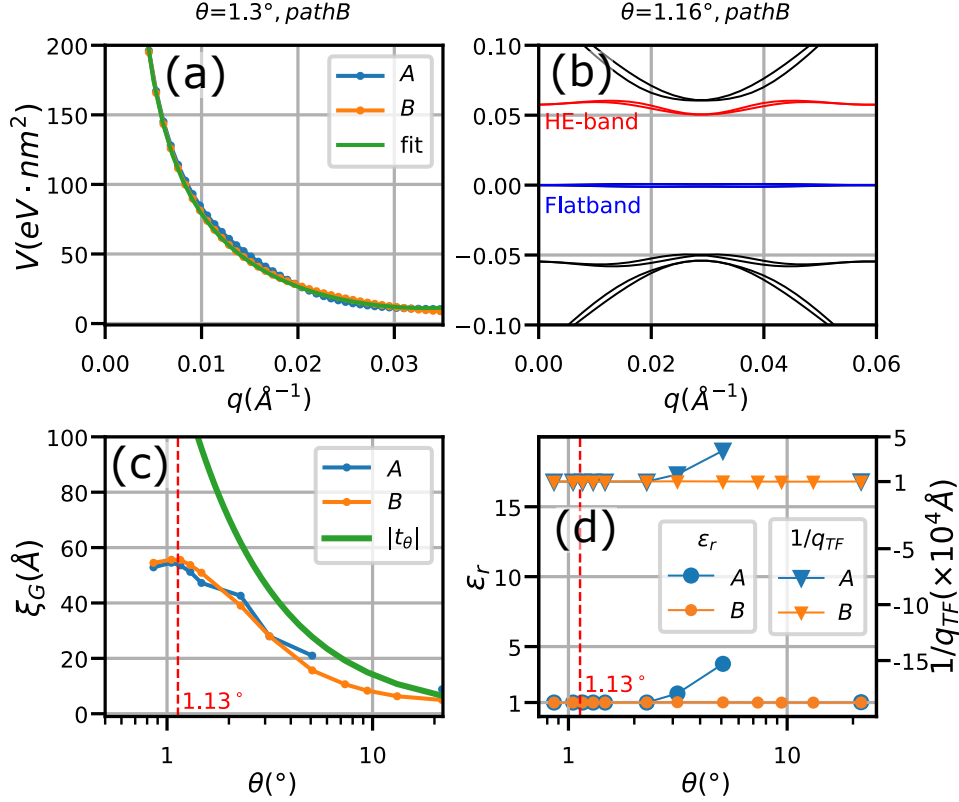


FIG. S2. Interaction matrix and its twist-angle dependence of the high-energy bands. (a) The interaction matrix for paths A and B , and the result of fitting (fit). (b) Band structure for the path B . The high-energy band is indicated by the red curve. (c) Angle dependence of radius ξ_G of Wannier function calculated for two paths A and B . The length of primitive vector $|t_\theta|$ is also plotted. (d) The angle dependence of ϵ_r and $1/q_{TF}$ calculated for the two paths. Angles where the fitting parameters are strongly affected by band crossings are excluded.

IV. INTERACTION MATRIX FOR THE OTHER BANDS

Here, we use a slightly different notation from the main text. An example is shown in Fig. S3 (a), which shows the dispersion of the flat bands for $\theta = 1.35^\circ$ along the path B in the main text. Here, we labeled the valence bands as $n = -2, -1$ and the conduction band as $n = 0, 1$. The bands are labeled in the ascending order of energy.

A. Flat bands

Figures S4(a-1)-S4(a-4) presents the interaction matrix $|V_{\mathbf{k},\mathbf{k}',\mathbf{q}}^{n_1,n_2,0,0}|$ for (n_1, n_2) corresponding to the flat bands, calculated along the path B at a twist angle $\theta = 1.35^\circ$; Fig. S4(a-1) shows the amplitude of the interaction between the two conduction-band electrons and Fig. S4(a-4) shows the amplitude of the interaction between conduction- and valence-band electrons. The intraband elements, $n_1 = n_3$ and $n_2 = n_4$, are essentially the only non-zero elements for $q < 0.03 \text{ \AA}^{-1}$, whereas the interband elements, $n_1 \neq n_3$ and $n_2 \neq n_4$, dominate for $q > 0.03 \text{ \AA}^{-1}$. This behavior can be explained by an anticrossing between the conduction and valence bands, which is at $q \sim 0.03$ in Fig S3.

In addition, Fig. S4(a-2) and S4(a-3) show the matrix elements that correspond to the amplitude of the scattering process in which one electron is scattered within the conduction bands and the other is scattered from the conduction bands to a valence band. In both cases, the values of $|V_{\mathbf{k},\mathbf{k}',\mathbf{q}}^{n_1,n_2,0,0}|$ lie between those shown in Fig. S4 (a-1) and (a-4).

Figures S4(b-1)-S4(b-4) and Fig. S4(c-1)-S4(c-4) presents the interaction matrix $|V_{\mathbf{k},\mathbf{k}',\mathbf{q}}^{n_1,n_2,n_3,n_4}|$ for (n_3, n_4) corresponding to the conduction bands. Despite the differences in the band indices (n_3, n_4) , the q -dependence of the interaction matrix shows a behavior similar to those of the conduction bands, including the anti-crossing effect. For example, the intraband elements shown in Fig. S4 (a-1), (b-1), and (c-1) show similar characteristics.

Figures S4(d-1)-S4(d-4) presents the interaction matrix $|V_{\mathbf{k},\mathbf{k}',\mathbf{q}}^{n_1,n_2,-1,-1}|$ for $(n_3, n_4) = (-1, -1)$, which corresponds to the valence bands. Here, Fig. S4(d-4) corresponds to the amplitude of the scattering within the valence bands. Similar

to the scattering amplitudes within the conduction bands, the intraband scattering element shown in Fig. S4(d-4) is the largest for $q < 0.03 \text{ \AA}^{-1}$, whereas the interband scattering element shown in Fig. S4(d-1) becomes prominent for $q > 0.03 \text{ \AA}^{-1}$.

Figure S5 shows the interaction matrix $|V_{\mathbf{k},\mathbf{k}',\mathbf{q}}^{n_1,n_2,n_3,n_4}|$ calculated along the path A for twist angle $\theta = 1.16^\circ$. Similar to Fig. S4, the interaction matrix shows a consistent pattern across different band indices. On the other hand, the interaction matrix in Figs. S5(a-4), S5(b-4), S5(c-4), and S5(d-1) shows a large interband scattering amplitude. This is caused by the enhancement of the backscattering along the path A .

B. High-energy band

The top rows of the Figure S6 display the band structure calculated along the path A for twist angles (a) $\theta = 21.79^\circ$, (b) 7.34° , (c) 5.09° , and (d) 3.15° . The bottom rows of the Figure S6 show corresponding interaction matrix $|V_{\mathbf{k},\mathbf{k}',\mathbf{q}}^{n_1,n_2,n_3,n_4}|$ calculated along the paths A and B for the high-energy band.

The amplitude of the interaction matrix calculated along path A for the twist angle $\theta = 7.34^\circ$ and 5.09° is much smaller than that calculated along path B . This is because the reconnection of the high-energy band occurs in these angles. For twist angle $\theta = 21.79^\circ$, the high-energy band plotted by red (HE-band) does not intersect with other bands near $q = 0$. However, for twist angle $\theta = 7.34^\circ$, The high-energy bands are approaching bands of even higher energy, leading to an anti-crossing near $q = 0.01 \text{ \AA}^{-1}$. Consequently, the amplitude of the scattering process straddling the anti-crossing is suppressed. Because of band reconnection, the interaction matrix for the high-energy band calculated along path A is much smaller than path B and the fitting doesn't work.

V. SUPPRESSION OF BACK SCATTERING IN THE DIRAC ELECTRONS

The amplitude $|V_{\mathbf{k},\mathbf{k}',\mathbf{q}}^{3,4,3,4}|$ for path A is smaller than those of paths B and C . This suppression resembles the suppression of backscattering in the Dirac electrons. For pristine graphene, eigenstate of the tight-binding hamiltonian reads

$$\psi_{\mathbf{k},\pm}(\mathbf{r}) = \frac{1}{\sqrt{2}}(g_{\mathbf{k}}\psi_{\mathbf{k},1}(\mathbf{r}) \pm \psi_{\mathbf{k},2}(\mathbf{r})), \quad g_{\mathbf{k}} = \frac{h_{\mathbf{k}}}{|h_{\mathbf{k}}|} \quad (\text{S5})$$

where $h_{\mathbf{k}} = t \sum_{i=1}^3 e^{i\mathbf{k} \cdot \mathbf{b}_i}$ with t being the nearest neighbor hopping, \mathbf{b}_i is vector connecting the three nearest neighbor sites in honeycomb lattice of pristine graphene and $\psi_{\mathbf{k},a}(\mathbf{r}) = \frac{1}{\sqrt{N_{\text{UC}}}} \sum_n e^{i\mathbf{k} \cdot \mathbf{R}_{n,a}} p_z(\mathbf{r} - \mathbf{R}_{n,a})$ with sublattice $a = 1, 2$; the sum is over all unit cells $\mathbf{R}_{n,a}$, and N_{UC} is the number of unit cells, $p_z(\mathbf{r})$ is the p_z orbital of the atom.

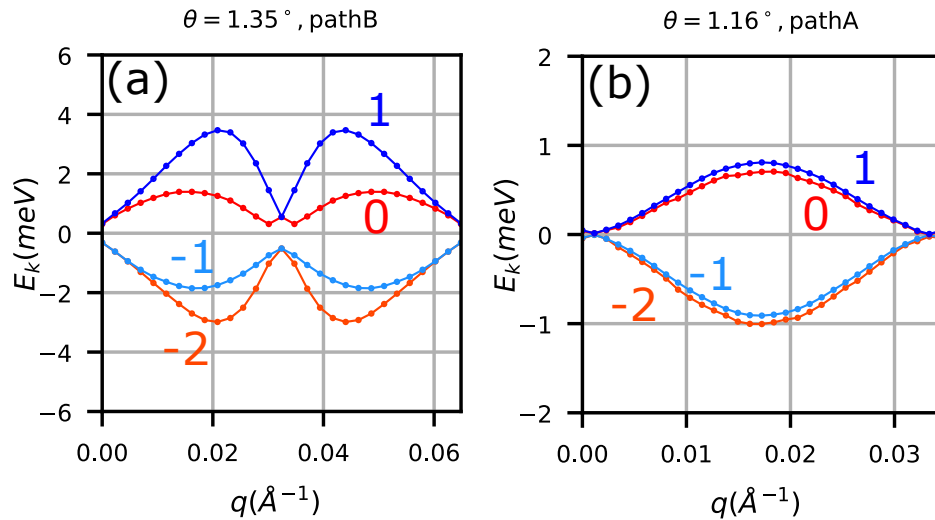


FIG. S3. The flat bands calculated along the path B at twist angle $\theta = 1.35^\circ$ (a) and along the path A at twist angle $\theta = 1.16^\circ$ (b). We labeled the bands in order of decreasing energy.

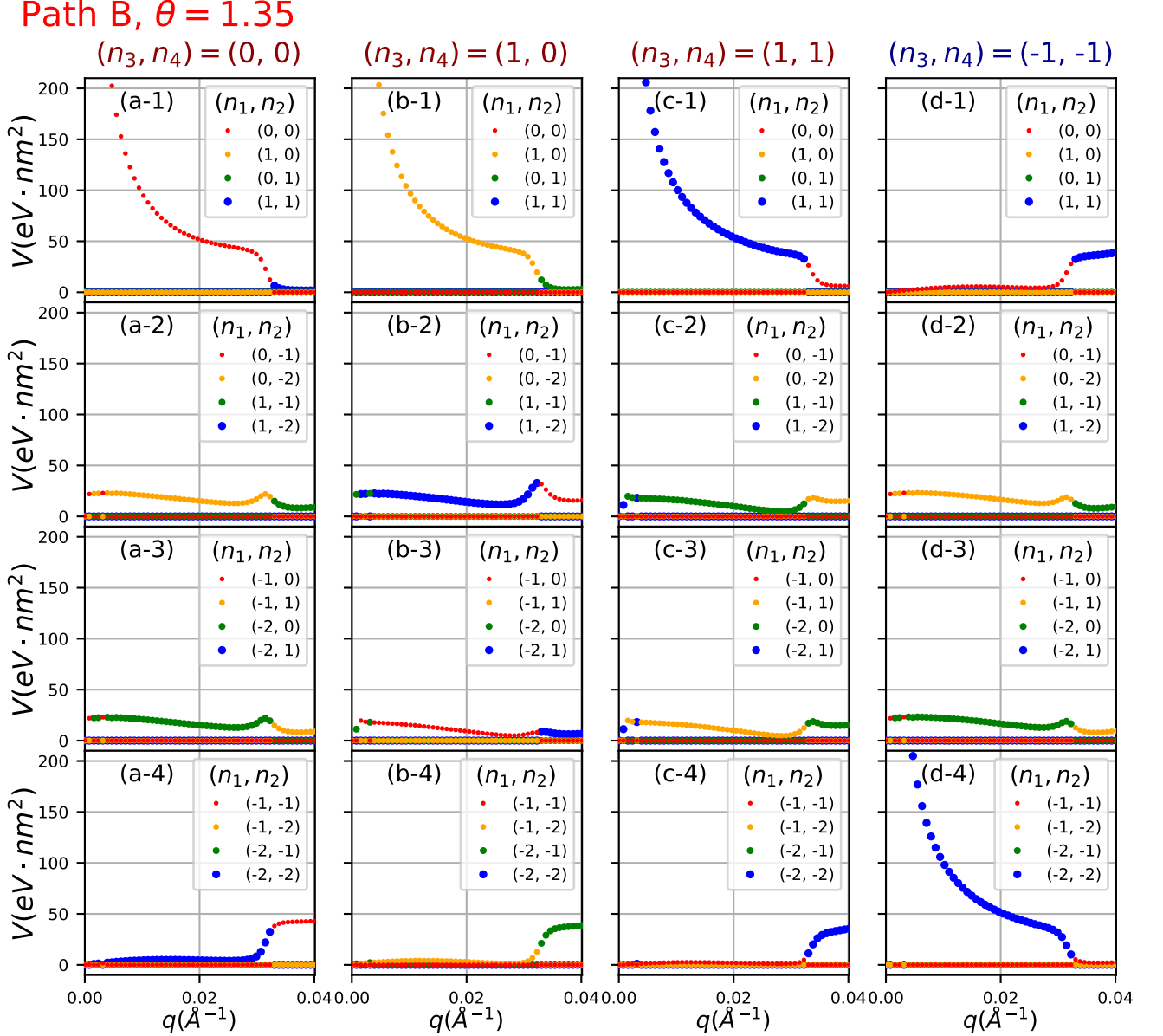


FIG. S4. $|V_{\mathbf{k}, \mathbf{k}', \mathbf{q}}^{n_1, n_2, n_3, n_4}|$ calculated along the path B at twist angle $\theta = 1.35^\circ$. The chosen band indices are $(n_3, n_4) = (0, 0)$ in (a-1)-(a-4), $(n_3, n_4) = (1, 0)$ in (b-1)-(b-4), $(n_3, n_4) = (1, 1)$ in (c-1)-(c-4), and $(n_3, n_4) = (-1, -1)$ in (d-1)-(d-4). All combinations of the band indices (n_1, n_2) chosen from the flat bands are plotted.

The amplitude depends on the factor $(g_{\mathbf{k}_1}^* g_{\mathbf{k}_2} + 1)$. For states near the Dirac point $\mathbf{K} = (\frac{4\pi}{3a}, 0)$, using $\tilde{\mathbf{k}} = \mathbf{k} - \mathbf{K}$, $g_{\mathbf{k}} \approx -e^{i\varphi_{\tilde{\mathbf{k}}}}$, where $\varphi_{\tilde{\mathbf{k}}} = \arg(\tilde{k}_x + i\tilde{k}_y)$. Thus, the factor reads $(g_{\mathbf{k}_1} g_{\mathbf{k}_2} + 1) \approx (e^{i(\varphi_{\tilde{\mathbf{k}}_2} - \varphi_{\tilde{\mathbf{k}}_1})} + 1)$. If two momenta $\mathbf{k}_1 = \mathbf{k} - \mathbf{q}$, and $\mathbf{k}_2 = \mathbf{k}$ are positioned at opposite sides of the Dirac point, $(g_{\mathbf{k}_1} g_{\mathbf{k}_2} + 1) \approx 0$ and the amplitude $|V_{\mathbf{k}, \mathbf{k}', \mathbf{q}}^{nmn'm'}|$ is suppressed. This is the suppression of the backscattering in the Dirac electrons.

VI. FITTING OF INTERACTION MATRIX NEAR THE MAGIC ANGLE

Figures S7(a) and S7(b) shows the interaction matrix of the conduction bands $V_{\mathbf{k}, \mathbf{k}', \mathbf{q}}^{3,4,3,4}$ at angles near the magic angle, $\theta = 1.16^\circ$ and $\theta = 1.05^\circ$, calculated using the microscopic model (fb+) and a fitted interaction matrix using the effective tight-binding model (fit). The interaction matrix for the effective tight-binding model is obtained by fitting the results of the microscopic model using ϵ , q_{TF} , and ξ_G as the fitting parameters. The effective tight-binding

Path A, $\theta = 1.16^\circ$

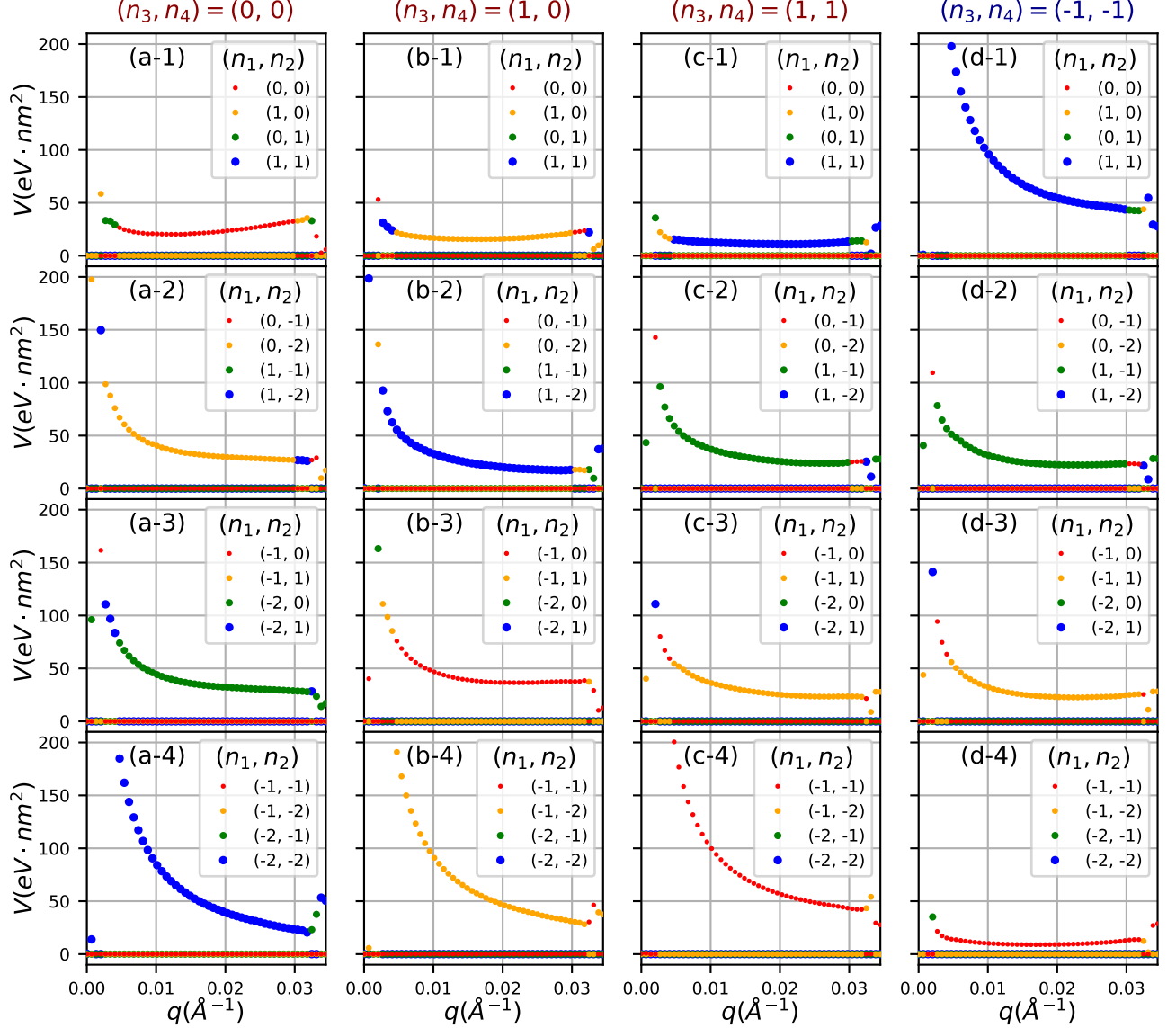


FIG. S5. $|V_{\mathbf{k},\mathbf{k}',\mathbf{q}}^{n_1,n_2,n_3,n_4}|$ calculated along the path A at twist angle $\theta = 1.16^\circ$. The chosen band indices are $(n_3, n_4) = (0, 0)$ in (a-1)-(a-4), $(n_3, n_4) = (1, 0)$ in (b-1)-(b-4), $(n_3, n_4) = (1, 1)$ in (c-1)-(c-4), and $(n_3, n_4) = (-1, -1)$ in (d-1)-(d-4). All combinations of the band indices (n_1, n_2) chosen from the flat bands are plotted.

model failed to reproduce the interaction matrix calculated by the microscopic model, especially for the range of small q . Also, the angle dependence of some of the fitting parameters show anomalous values around the magic angle. In addition, the fitting parameters considerably vary depending on the path. For example, at the twist angle $\theta = 1.16^\circ$, the radius is $\xi_G \sim 0.7 \text{ \AA}$ for the path A, while it is $\xi_G \sim 20$ for the paths B and C. The inconsistencies suggest a failure of the fitting.

-
- [1] C H Xu, C Z Wang, C T Chan, and K M Ho, “A transferable tight-binding potential for carbon,” *Journal of Physics: Condensed Matter* **4**, 6047 (1992).
 - [2] G. Trambly de Laissardière, D. Mayou, and L. Magaud, “Localization of dirac electrons in rotated graphene bilayers,” *Nano Letters* **10**, 804–808 (2010).

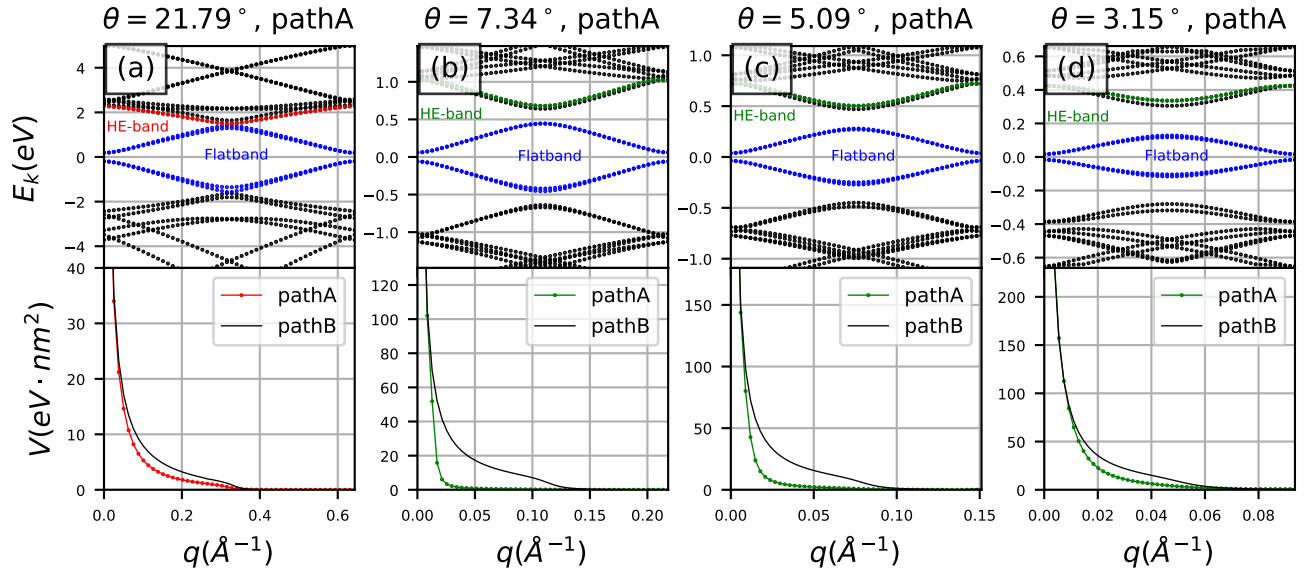


FIG. S6. Band structure calculated along path A (top row) and the corresponding interaction matrix (bottom row). The twist angle is $\theta = 21.79^\circ, 7.34^\circ, 5.09^\circ$ and 3.15° for (a), (b), (c) and (d) respectively.

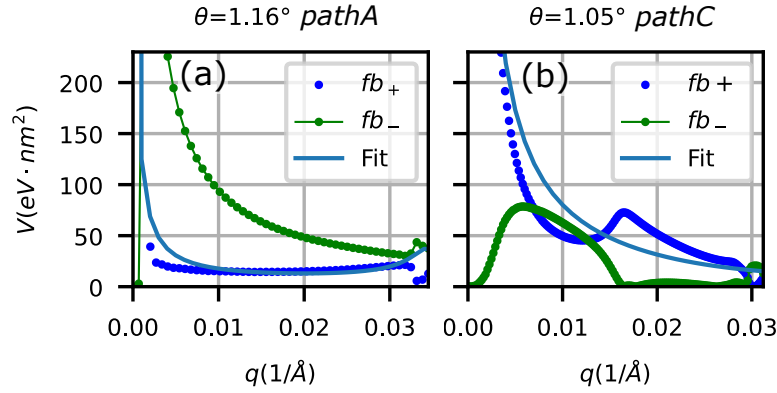


FIG. S7. Fitting of the interaction matrix for the flat bands by using a Gaussian Wannier function. (a,b) The interaction matrix corresponds to scattering from the conduction to the conduction band (fb_+), the interaction matrix corresponds to scattering from the conduction to the valence band (fb_-), and the fitting function for fb_+ (fit). The results are for paths A (a) and C (b).

- [3] J. C. Slater and G. F. Koster, "Simplified lcao method for the periodic potential problem," Phys. Rev. **94**, 1498–1524 (1954).
- [4] G. Trambly de Laissardière, D. Mayou, and L. Magaud, "Numerical studies of confined states in rotated bilayers of graphene," Phys. Rev. B **86**, 125413 (2012).
- [5] Artur L. Shilov, Mikhail A. Kashchenko, Pierre A. Pantaleón Peralta, Yibo Wang, Mikhail Kravtsov, Andrei Kudriashov, Zhen Zhan, Takashi Taniguchi, Kenji Watanabe, Sergey Slizovskiy, Kostya S. Novoselov, Vladimir I. Fal'ko, Francisco Guinea, and Denis A. Bandurin, "High-mobility compensated semimetals, orbital magnetization, and umklapp scattering in bilayer graphene moiré superlattices," ACS Nano **18**, 11769–11777 (2024).